Journal of Power Sources 205 (2012) 324–334

Contents lists available at SciVerse ScienceDirect

Journal of Power Sources

journal homepage: www.elsevier.com/locate/jpowsour

Degradation of a PEM fuel cell stack with Nafion® membranes of different thicknesses. Part II: Ex situ diagnosis

Xiao-Zi Yuan[a,*], Shengsheng Zhang[a], Shuai Ban[a], Cheng Huang[a], Haijiang Wang[a,**], Vengatesan Singara[b], Michael Fowler[b], Mathias Schulze[c], Andrea Haug[c], K. Andreas Friedrich[c], Renate Hiesgen[d]

[a] Institute for Fuel Cell Innovation, National Research Council Canada, Vancouver, BC, Canada V6T 1W5
[b] Department of Chemical Engineering, University of Waterloo, 200 University Avenue West, Waterloo, ON, Canada N2L 3G1
[c] Institute of Technical Thermodynamics, German Aerospace Center, Pfaffenwaldring 38-40, 70569 Stuttgart, Germany
[d] University of Applied Sciences Esslingen, Department of Basic Science, Kanalstrasse 33, 73728 Esslingen, Germany

ARTICLE INFO

Article history:
Received 13 October 2011
Received in revised form 7 January 2012
Accepted 12 January 2012
Available online 21 January 2012

Keywords:
Proton exchange membrane fuel cell
Stack
Ex situ
Durability
Idle conditions
Degradation

ABSTRACT

Part I of this study carried out membrane electrode assembly degradation of a four-cell stack with Nafion membranes of different thicknesses, including N117, N115, NR212, and NR211, for 1000 h under idle conditions. Through on-line electrochemical measurements it was found that as degradation advanced, cells with thinner membranes experienced much more rapid performance degradation than those with thicker membranes, especially after 800 h of operation, due to a dramatic increase in hydrogen crossover. In the present work we investigate the degradation mechanisms of this four-cell stack using several ex situ diagnostic tools, including scanning electron microscopy (SEM), infrared (IR) imaging, ion chromatography (IC), gas permeability measurement, contact angle measurement, and simulation. The results indicate that the drastic increase in hydrogen crossover is due to membrane thickness loss and pinhole formation.

1. Introduction

The durability of proton exchange membrane (PEM) fuel cells is one of the biggest challenges and barriers for commercializing this promising technology. The 2015 US Department of Energy lifetime requirements for transportation applications range from 5000 h for cars to 20,000 h for buses, and for stationary applications the requirement is 40,000 h of continuous operation. Currently, the lifetimes of fuel cell vehicles and stationary cogeneration systems are around 1700 h and 10,000 h, respectively [1]. Accordingly, continuous R&D on the issues related to PEM fuel cell durability is still required to gain a fundamental understanding of degradation mechanisms, which in turn will help reduce the technology gap and provide mitigation strategies.

PEM fuel cells consist of many components, including catalysts, catalyst supports, membranes, gas diffusion layers (GDLs), bipolar plates, sealings, and gaskets. Each of these components can degrade or fail to function, thus causing the fuel cell system to degrade or fail. So far, various failure modes of component degradation have been identified, such as catalyst particle agglomeration/dissolution, carbon support oxidation, membrane dissolution, ionomer degradation in the catalyst layer (CL), hydrophobicity changes in the CL and/or GDL, and PTFE decomposition in the CL and/or GDL. Depending on internal factors (e.g., material properties, and the design of the components and the stack) and external factors (e.g., fuel cell operating conditions, impurities or contaminants in the feeds, and environmental conditions), one or several failure modes are predominant over the others [2].

Generally, it is impractical and costly to operate a fuel cell under its normal conditions for several thousand hours; accelerated test methods are thus preferred to facilitate rapid learning about key durability issues. The US Department of Energy has established accelerated stress test (AST) protocols for cell components, including electrocatalysts, catalyst supports, membranes, and membrane electrode assemblies, in an attempt to provide a standard set of test conditions and operating procedures to evaluate new cell component materials and structures [3]. Different research groups may prefer their own test protocols or design special degradation tests to investigate failure modes, with a special target in mind. For example, as the idle time may amount to several thousand hours over

* Corresponding author. Tel.: +604 221 3000x5576.
** Corresponding author. Tel.: +604 221 3038; fax: +604 221 3001.
E-mail addresses: xiao-zi.yuan@nrc.gc.ca (X.-Z. Yuan), haijiang.wang@nrc-cnrc.gc.ca (H. Wang).

0378-7753/$ – see front matter. Crown Copyright © 2012 Published by Elsevier B.V. All rights reserved.
doi:10.1016/j.jpowsour.2012.01.074

the entire lifetime of a fuel cell, it is considered one of the most crucial factors affecting the cell's durability, especially for automotive fuel cell systems [4,5]. Wu et al. [6] conducted a six-cell stack degradation procedure under close to open circuit voltage (OCV) conditions, finding considerable hydrogen crossover after 800 h of operation. To facilitate membrane degradation studies, Yuan et al. [7] reported an accelerated degradation test involving a four-cell stack degradation procedure using Nafion membranes of different thicknesses, including N117, N115, NR212, and NR211, for 1000 h under idle conditions. The cell performance and electrochemical characteristics were monitored approximately every 200 h of operation.

While various ASTs are designed and performed on PEM fuel cells, numerous diagnostic tools, including in situ and ex situ tools, are implemented to interpret experimental results, to investigate failure modes, and to gain a fundamental understanding of component degradation. To date, a wide range of experimental diagnostic tools for the accurate analysis of PEM fuel cells and stacks have been developed, as reviewed by Wu et al. [8,9]. For example,

- Atomic force microscopy (AFM) – Nanoscale Nafion membrane and GDL degradation [10,11]
- Infrared (IR) imaging – Membrane thinning and pinhole detection [12,13]
- X-ray diffraction (XRD) – Particle size change [14] and loss of surface area [15]
- Scanning electron microscopy (SEM) – Morphological changes [16] and degradation of membrane [17], CL [18], and GDL [19]
- Transmission electron microscopy (TEM) – Diagnosis of electrocatalyst degradation [20]
- Fourier transform infrared spectroscopy (FTIR) – Polymer alterations induced by degradation [21]
- X-ray photoelectron spectroscopy (XPS) – Surface component loss [22]
- Ion chromatography (IC) – Membrane and ionomer degradation through analysis of dissolved fluoride ions [23,24].

These ex situ tools play an important role in investigating failure modes and degradation mechanisms.

Previously, we performed an in situ diagnosis of a four-cell stack with membranes of different thicknesses, where traditional electrochemical diagnostic tools (including OCV, polarization curve, electrochemical impedance spectroscopy (EIS), and linear sweep voltammetry (LSV)) were used to observe performance losses after 1000 h of operation under idle conditions [7]. In the present work, an ex situ diagnosis is carried out to identify the major failure mode. These ex situ measurements include SEM, IR imaging, IC, gas permeability measurement, and contact angle measurement.

2. Experimental

2.1. Fuel cell materials and test apparatus

The fuel cell tested was a four-cell stack with an active area of 50 cm^2. The materials used were Ion Power customized catalyst coated membranes (CCMs) (N117, N115, NR212, and NR211) with a Pt catalyst loading of 0.3 mg cm^{-2}, supported on carbon on both sides, and SGL GDLs. During the degradation test, the four-cell stack was operated at a constant current of 0.5 A (10 mA cm^{-2}). The fuel cell stack temperature was kept at 70 °C, and air and hydrogen were fully humidified prior to their delivery into the fuel cell. Detailed procedures of this stack degradation test, as well as electrochemical measurements, have been described in the literature [7].

2.2. Ex situ diagnosis

2.2.1. SEM

Cross-sectional SEM images were taken using a HITACHI S-3500N before and after degradation to identify morphological changes as well as thickness changes in the membrane and CLs. All the samples used for SEM scanning, including fresh and degraded NR211, NR212, N115, and N117, were cut from 50 cm^2 sheets into 10 mm × 20 mm pieces. These pieces were then fractured after immersion in liquid nitrogen.

2.2.2. IC

The fluoride content of the water samples collected from the anode and cathode at the beginning of test (BOT) and end of test (EOT) was analyzed using an ion chromatograph (Dionex DX 500) with an electrochemical detector (Dionex ED 40) and working with a gradient pump (Dionex GP 40). The analytical column used to separate the fluoride ions from other anions was a Dionex AS17 plus AG17 guard column, and 20 mM NaOH was used as the eluent. Based on the relative exchange of anions between the stationary column and mobile phase, the anions were eluted and detected at different time intervals, making the chromatogram. The minimum detectable limit of fluoride ions in the sample was 0.011 mg L^{-1}.

2.2.3. IR imaging

To detect pinholes generated in the membranes after degradation, IR imaging was carried out to observe the location of higher hydrogen crossover, reflected by the temperature distribution on the membrane electrode assembly (MEA), which is based on the heat output from the chemical reaction between hydrogen (crossed over from the anode) and oxygen in the presence of Pt catalyst [12]. The temperature distribution obtained from IR images demonstrates the level of reactant crossover through the PEM. For comparison, the same test was also conducted on a fresh MEA.

IR imaging was performed using an IR camera (InfraTech GmbH) and a specially designed cell (50 cm^2) with an open cathode, which provided sufficient air for the reaction. The anode required a diluted hydrogen supply (e.g., 5% H_2 in N_2, Linde). The entire experimental set-up included a hydrogen cylinder, hydrogen regulator, flow meter, dummy cell, IR camera, and computer. The entire piece of fresh or degraded MEA was installed in the self-designed cell, with diluted hydrogen passing through the anode at a flow rate of 30 sccm min^{-1} at room temperature and a pressure of 5 psi. The IR camera was placed towards the open cathode to observe the temperature distribution.

2.2.4. Gas permeability

Selective permeability of gases through the membrane is an easy and viable method to investigate membrane failures, such as rips, tears, cracks, and pinholes. An impulsive increase in permeability may be expected after a long-term AST. During this experiment, selective gases, such as He, N_2, or Ar, which have different molecular sizes, were fed into the anode side of the cell, and the gas flux across the membrane was measured at the cathode. This can be done for both fresh and degraded samples. By using different gases and their selective permeability, one can distinguish whether the permeation is related to the solution or to Knudson behavior. The apparent permeability (P_M) of the membrane was calculated using Fick's law (1):

$$N_A = \frac{P_M (P_I - P_{II})}{l} \quad (1)$$

where P_I and P_{II} are the partial pressures of the analyte gas at either side of the membrane, and N_A is the flux of gas molecules across the membrane with a finite thickness (l). It is assumed that the gas flux through the membrane will increase if the membrane

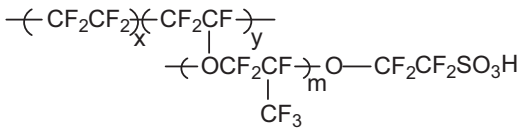

Fig. 1. Chemical structure of Nafion. In this work, the equivalent weight is chosen to be about 1100 g of dry Nafion per mole of sulfonic acid groups, with $x = 6.5$ and $y = m = 1$.

thickness changes due to thinning and/or the presence of membrane pinholes, tears, or cracks.

2.2.5. Contact angle

Contact angle measurement was conducted on a Kitchener 519-748-4612 from FOLIO Instruments Inc., and the water drop image taken and the angle fitting program used was FTA32. For contact angle observation of the GDLs, two pieces (10 mm × 10 mm) were cut from each fresh and degraded sample sheets for both the anode and cathode, and then three different spots were measured on each sample. All the samples were stuck onto a glass substrate using a double-sided sticker. To observe the contact angle for the CLs, the GDL layers were peeled off carefully with the help of a scalpel. Note that for each sample we chose at least three locations, and each image was fitted at least three times. Therefore, the final result for the contact angle is an average value for each sample.

Note that for each of the ex situ tests, we used the same fresh and degraded samples. IR imaging and gas permeability measurements were performed before cutting the samples for SEM and contact angle observations. The "fresh" samples were the ones that have been compressed and conditioned without any further operation as described in our previous publication [7].

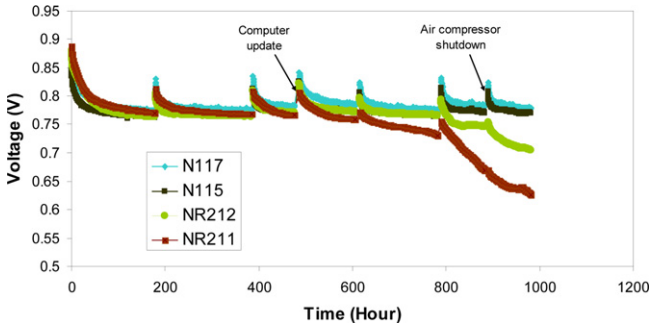

Fig. 2. Voltage degradation trends for individual cells under idle conditions for 1000 h (operating conditions: flow rate H_2/air = 1/2 slpm, cell temperature 70 °C and fully humidified on both sides).

2.3. Simulation methods

The kinetic Monte Carlo (KMC) method was used to model the main chain unzipping process [25,26]. In this method, all possible events or simulation steps are considered independent for all

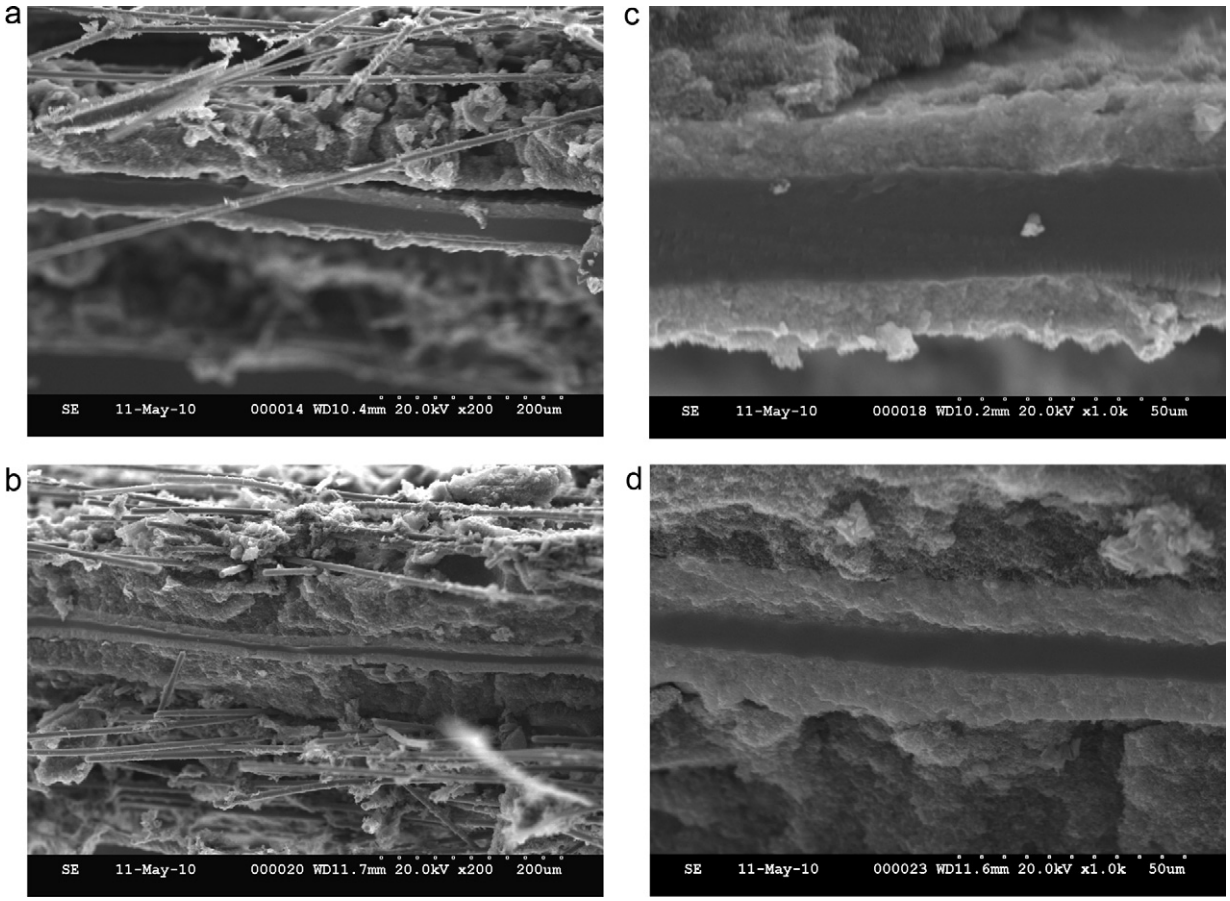

Fig. 3. Comparison of SEM images for NR211 samples before and after degradation, at different magnifications: (a) before degradation, at a magnification of 200×, (b) after degradation, at a magnification of 200×, (c) before degradation, at a magnification of 1.0k×, and (d) after degradation, at a magnification of 1.0k×.

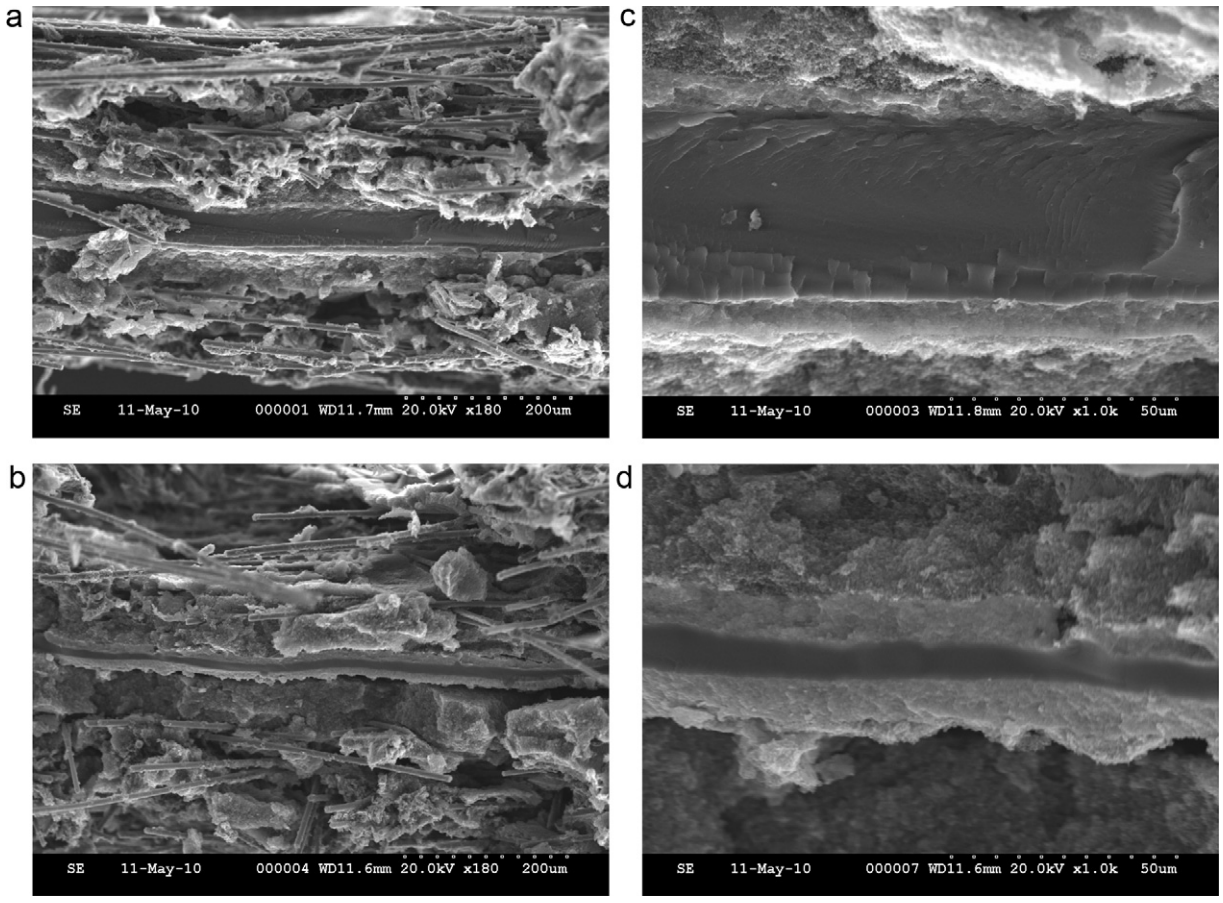

Fig. 4. Comparison of SEM images for NR212 samples before and after degradation, at different magnifications: (a) before degradation, at a magnification of 180×, (b) after degradation, at a magnification of 180×, (c) before degradation, at a magnification of 1.0k×, and (d) after degradation, at a magnification of 1.0k×.

Nafion atoms. A certain event is selected with a probability proportional to its rate. In particular, the carboxyl groups are assumed to be the major reactant, with a rate constant of 1. The Arrhenius equation

$$k = A \exp\left(\frac{E_a}{RT}\right) \quad (2)$$

is often used to derive the rate constants from the reaction enthalpy calculated by density function theory [27]. As the pre-exponential term A is not determined explicitly in this work, the processing time calculated by KMC has an arbitrary unit. The chemical structure of Nafion is shown in Fig. 1 [28]. In the present work, a Nafion polymer consisted of 20 monomers, namely 20 side chains and 300 CF_x groups in the PTFE backbone. In total, 1000 Nafion chains were used. The concentration of peroxide radicals $OH^{\bullet}$ was assumed to be constant [27]. By neglecting the formation procedure of free radicals in accelerated stress test we may have slightly overestimated the quantity of radicals in the initial stage, where ionomer dissolution may have taken place less rapidly than we modeled [27]. A typical simulation was started from a network of Nafion ionomers partially terminated with carboxyl end groups, with a maximum of two per Nafion chain. After the execution of this event, the list of possible events was updated and the procedure was repeated until the desired weight loss of Nafion was reached. Statistical data for the degradation products was collected during the whole process.

3. Results and discussion

3.1. Summary of in situ results

Based on the previous in situ diagnosis, the OCV of the individual cells decreases much faster for thinner membranes, especially after 800 h of operation. Before degradation, the thinner the membrane is, the higher the cell performs. However, as degradation progresses, the cells with thinner membranes degrade much faster. Fig. 2 shows the voltage degradation curves of each individual cell of the stack up to 1000 h under idle conditions. As can be seen, from 600 to 800 h the cell with the NR211 membrane degrades significantly, whereas the other cells do not experience drastic degradation; from 800 to 1000 h, both cells with thinner membranes (NR211 and NR212) degrade dramatically, while the two cells with thicker membranes (N115 and N117) still retain a slight degradation rate. Fig. 2 yields an average degradation rate of approximately 0.18 mV h^{-1} for NR212 and 0.26 mV h^{-1} for NR211, and of approximately 0.09 mV h^{-1} for both N115 and N117. Note that the voltage jumps were caused by interruptions of the degradation process for electrochemical measurements at 200 h intervals or unexpected shutdowns of the test station as indicated in the figure. Based on the linear sweep voltammetry (LSV) curves measured after each 200 h, increased hydrogen crossover was found to be responsible for the drastic performance loss for cells with thinner membranes [7]. This is in agreement with our previous degradation test under idle conditions [6]. The results indicate that

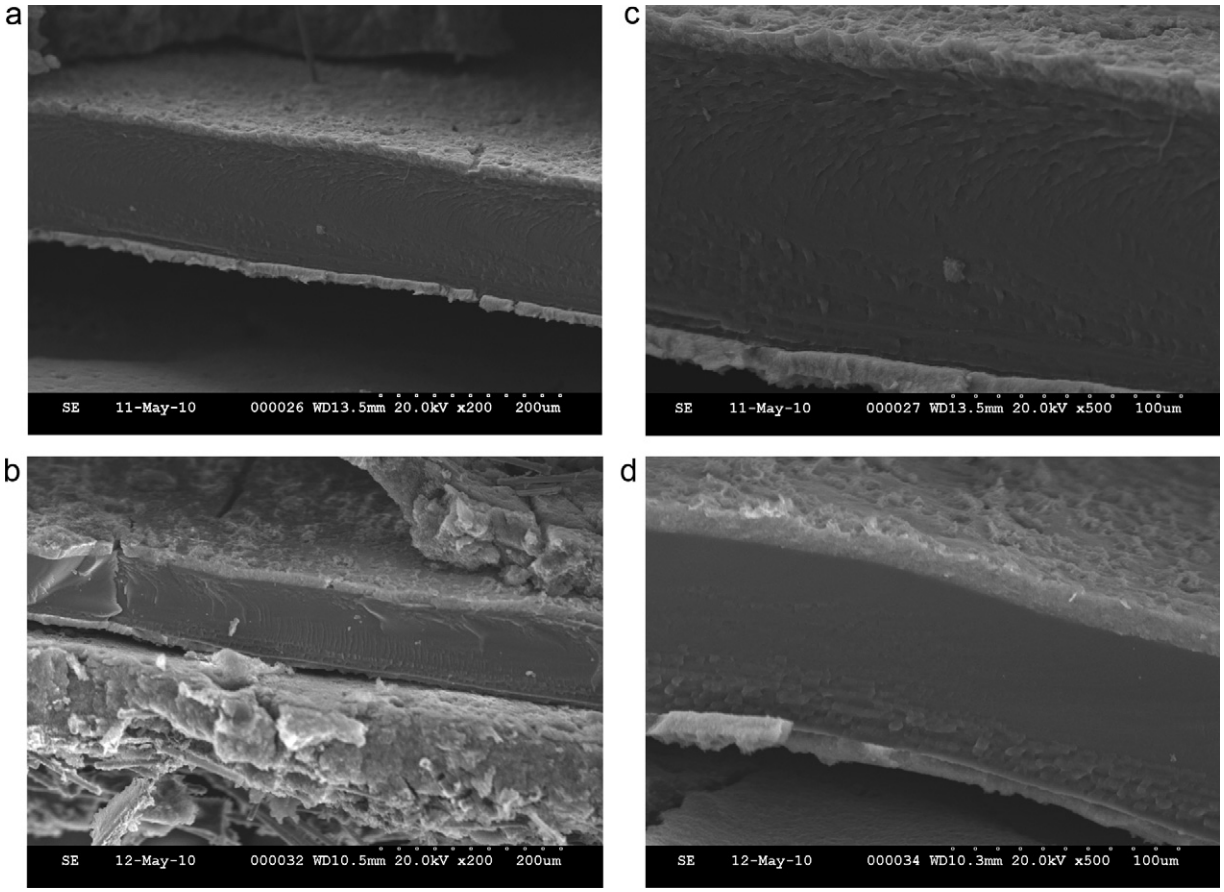

Fig. 5. Comparison of SEM images for N115 samples before and after degradation, at different magnifications: (a) before degradation, at a magnification of 200×, (b) after degradation, at a magnification of 200×, (c) before degradation, at a magnification of 500×, and (d) after degradation, at a magnification of 500×.

membrane degradation is the major source of the entire cell performance degradation under idle conditions. It was assumed that membrane thinning or pinhole formation was responsible for the increased hydrogen crossover [7].

3.2. Ex situ results

3.2.1. Thickness loss

Figs. 3–6 show the respective SEM images for NR211, NR212, N115, and N117 samples before and after degradation, at different magnifications. Macroscopically, obvious thickness decrease is observable after 1000 h of degradation under idle conditions, especially for thin membranes. We measured the thickness changes for all the membranes; the results are listed in Table 1.

As shown in Table 1, there is a 3–4 μm difference in membrane thickness between the fresh samples and samples conditioned by cell compression (100 psi). After degradation, membrane thickness decreases significantly, especially for thin membranes, with a total thickness loss of 66% for NR211 and 68% for NR212. However, this does not mean that thin membranes degrade faster. Thickness losses for thin membranes are still lower than for thick membranes, since there is less Nafion in the thin membranes to degrade. We believe that for thin membranes, only a small fraction of the membrane needs to degrade to observe a crossover increase and subsequent OCV decrease.

Table 1
Membrane thickness change before and after degradation.

	Fresh (μm)	After conditioning (μm)	Degraded after 1000 h (μm)	Thickness lost (μm)	Thickness decrease (%)
NR211	25.4	22	7.5	14.5	66
NR212	50.8	44	14	30	68
N115	127	124	78	46	37
N117	183	179	142	37	21

As analyzed by Collier et al. [29], the causes of membrane degradation include mechanical degradation, thermal degradation, and chemical and electrochemical degradation. We believe that dramatic membrane thickness loss or membrane thinning can be attributed to radical attacks, a mechanism proposed by Curtin et al. [26]. As radicals formed at the anode will attack H-containing end groups, Nafion membrane degradation begins with the abstraction of hydrogen. The formed perfluorocarbon radical can then react with a hydroxyl radical to produce HF and an acid fluoride. The final step includes hydrolysis of the acid fluoride:

$$\text{(i)R-CF}_2\text{COOH} + {}^{\bullet}\text{OH} \rightarrow \text{R-CF}_2{}^{\bullet} + \text{CO}_2 + \text{H}_2\text{O} \quad (3)$$

$$\text{(ii)R-CF}_2{}^{\bullet} + {}^{\bullet}\text{OH} \rightarrow \text{R-CF}_2\text{OH} \rightarrow \text{R-COF} + \text{HF} \quad (4)$$

$$\text{(iii)R-COF} + \text{H}_2\text{O} \rightarrow \text{R-COOH} + \text{HF} \quad (5)$$

The water samples were analyzed using IC. This analysis of the fluoride concentration in water from the stack outlets may be essential in revealing the level of membrane dissolution and ionomer loss in the CL. The result shows that fluorine emission rates increased dramatically from 2.2 mg L^{-1} and 2.4 mg L^{-1} at BOT to 11.9 mg L^{-1} and 10.3 mg L^{-1} at EOT for the anode and cathode of the stack, respectively. Therefore, the tremendous thickness loss in the membranes was further confirmed by the fluorine release measured by IC. Unfortunately, this technique could not detect fluorine release rates for individual cells.

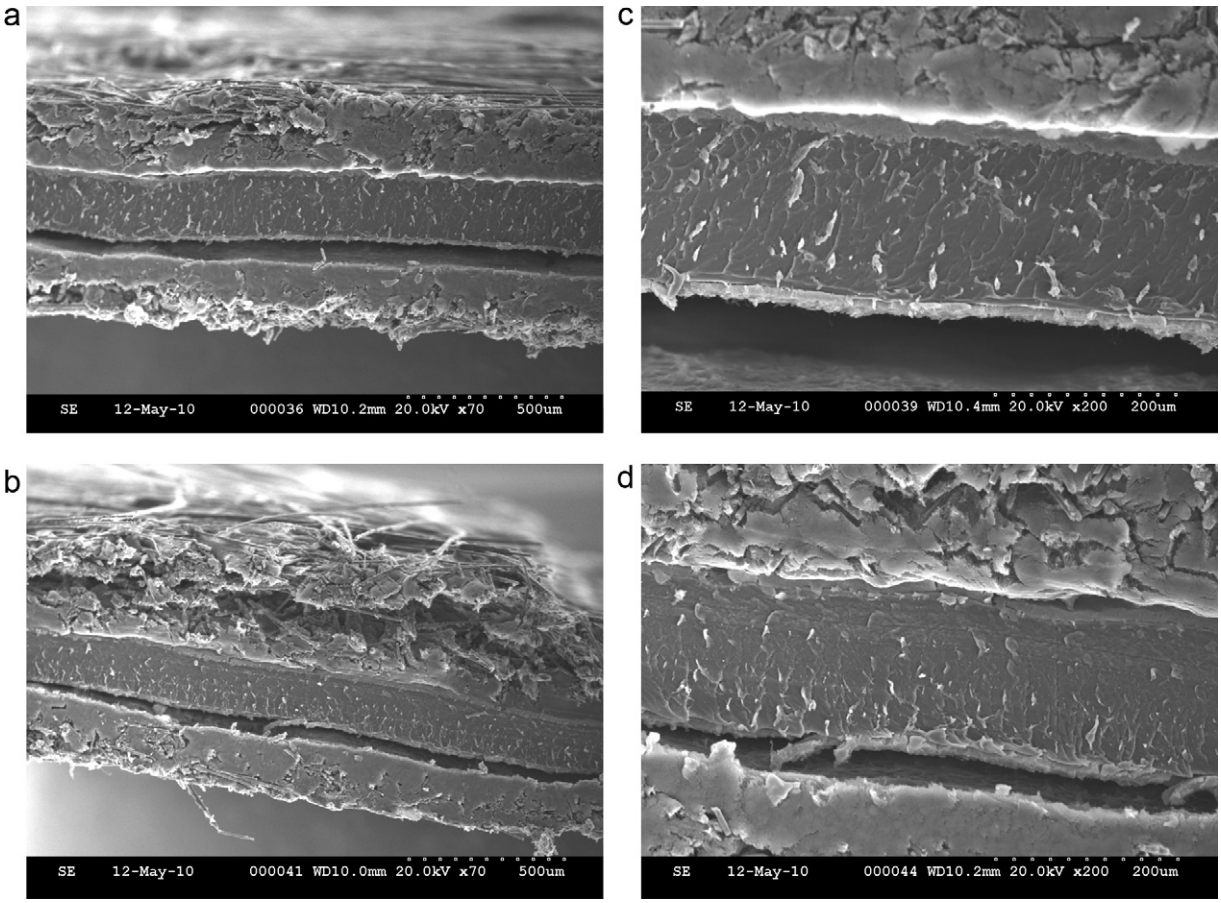

Fig. 6. Comparison of SEM images for N117 samples before and after degradation, at different magnifications: (a) before degradation, at a magnification of 70×, (b) after degradation, at a magnification of 70×, (c) before degradation, at a magnification of 200×, and (d) after degradation, at a magnification of 200×.

From our SEM images, we also measured the thickness changes in the CLs; the results are listed in Table 2. We found that: the CL thicknesses for both electrodes were between 9 and 13 μm before and after degradation; no obvious cathode CL thinning was identifiable; and a thickness loss of about 1–2 μm was observable for the anode CL, but the change was not significant. The CL loss is attributable to Pt dissolution/migration/washout and ionomer loss, as observed by fluoride release. It is still unclear why the anode lost more catalyst than the cathode.

3.2.2. Pinhole formation

Fig. 7(a)–(d) compares four fresh MEAs with different membranes. As can be seen from the four images, temperature is evenly distributed throughout the MEA for all the fresh samples with different membranes. No obvious hot spot can be observed, even for the thinnest membrane. However, from the color or average temperature of each sample, we can conclude that the thinner the membrane, the higher the average temperature and the greater the hydrogen crossover through the membrane, which agrees perfectly with the results from LSV in our previous publication [7]. Apparently, hydrogen crossover through membranes, as well as membrane thicknesses, can be compared or determined qualitatively using IR imaging.

Table 2
Catalyst layer thickness change before and after degradation.

	Anode after conditioning (μm)	Cathode after conditioning (μm)	Anode after degradation (μm)	Cathode after degradation (μm)
NR211	11–12	11–12	10–11	11
NR212	9–10	9–10	8–9	10–11
N115	11–12	11–12	9–10	11–12
N117	13	13	11	13

Figs. 8–11 compare IR images for MEA samples with different membranes before and after degradation. For thicker membranes (N117 and N115) there is a very slight increase in the average temperature, as shown by the color change in the images. However, this temperature/crossover change is not at all significant before or after degradation, which matches the slight performance decay observed from the polarization curve. For thinner membranes (NR212 and NR211), hydrogen crosses over significantly through a weak area or pinholes after 1000 h of operation under idle conditions. This result agrees very well with the LSV curves described in our previous paper, and explains the OCV degradation, as well as the performance degradation measured by the polarization curves. We further speculate that for thinner membranes, pinholes are the major reason for membrane degradation, rather than membrane thinning, indicated by a slight increase in the background temperature.

The formation of pinholes can be explained as a comprehensive effect of the aforementioned membrane degradation mechanisms. Radicals formed from electrochemical reactions attack the membrane, causing losses of hydrogen, fluorine, sulfur, and end groups, which is a direct reason for membrane thinning. A thinner membrane leads to more hydrogen crossover, which further worsens the situation. Also, the crossed hydrogen may react with oxygen, causing local heat stress. Together, the continuous radical attacks, heat stress, and mechanical stress arising from the wettability change lead to pinhole formation.

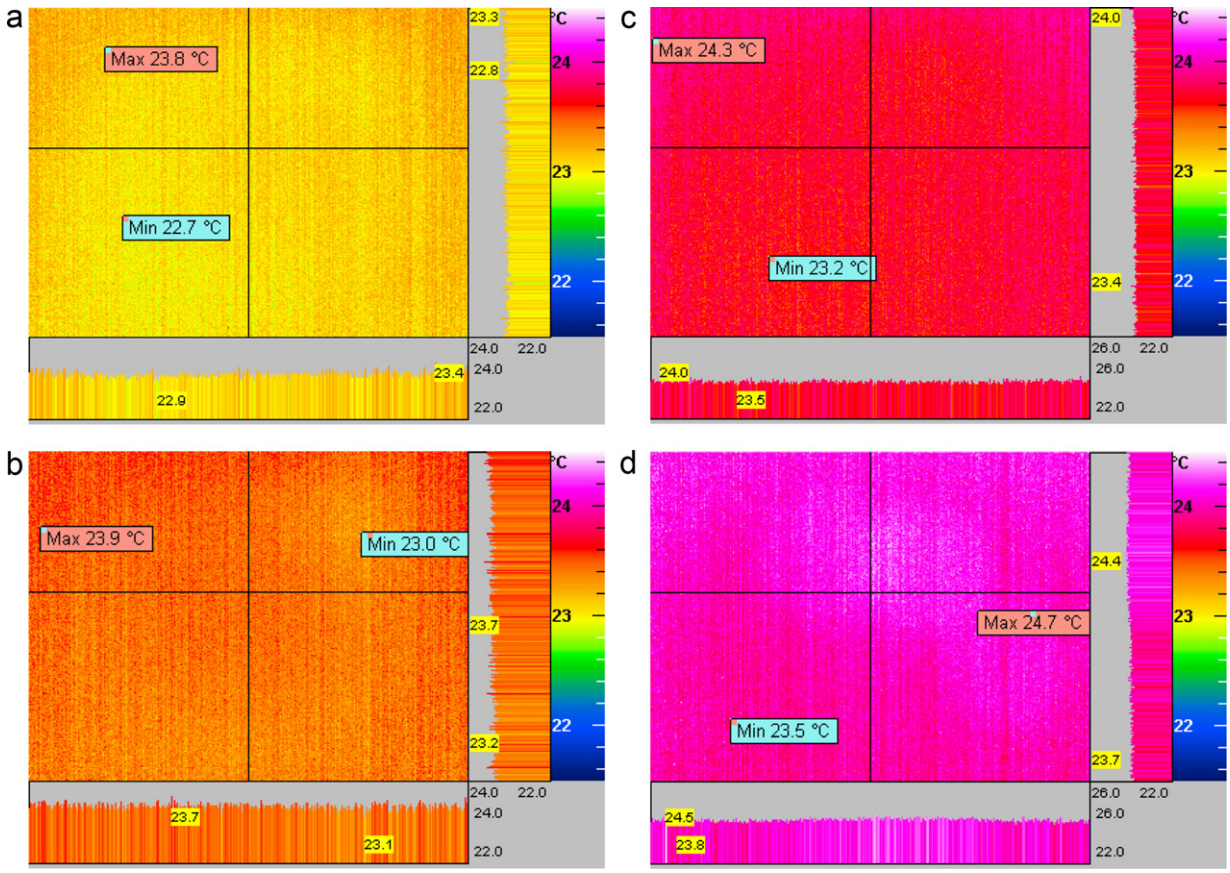

Fig. 7. Comparison of IR images for fresh MEA samples with different membranes using 5% H_2 in N_2: (a) fresh N117 MEA (average temp: 23.091 °C), (b) fresh N115 MEA (average temp: 23.429 °C), (c) fresh NR212 MEA (average temp: 23.724 °C), and (d) fresh NR211 MEA (average temp: 24.063 °C).

To further confirm that pinholes do exist after 1000 h of membrane degradation testing for thinner membranes, we also designed a different measurement using the same IR imaging set-up to visually observe pinholes. Instead of employing an IR camera for the cathode, we put a certain amount of deionized water on top of the open cathode, with hydrogen passing through the anode channel of the cell at a pressure of 5 psi and a flow rate of 30 sccm min^{-1}. No water bubbles were observable for the fresh samples, or for the degraded N117 and N115 samples after 1000 h of degradation. Bubbles were observed for the degraded NR212 and NR211 MEAs, as shown in Fig. 12. Unfortunately, the bubble locations do not exactly match the locations of the hot spots observed from IR images. This can be explained by the porous nature of GDLs, as the hydrogen crossing over through pinholes prefers an easier path through the GDL (not necessarily right in line with the pinholes).

Further proof of pinhole formation can be obtained through a gas permeability test. Fig. 13 shows the permeability of helium through highly permeable and less permeable MEAs, defined thus:

- non-permeable: no gas flow across the MEA until 50 psi
- less permeable: very low gas flow, indicated by bubble formation at longer intervals
- highly permeable: considerable gas flow across the MEA, measured by rotameter

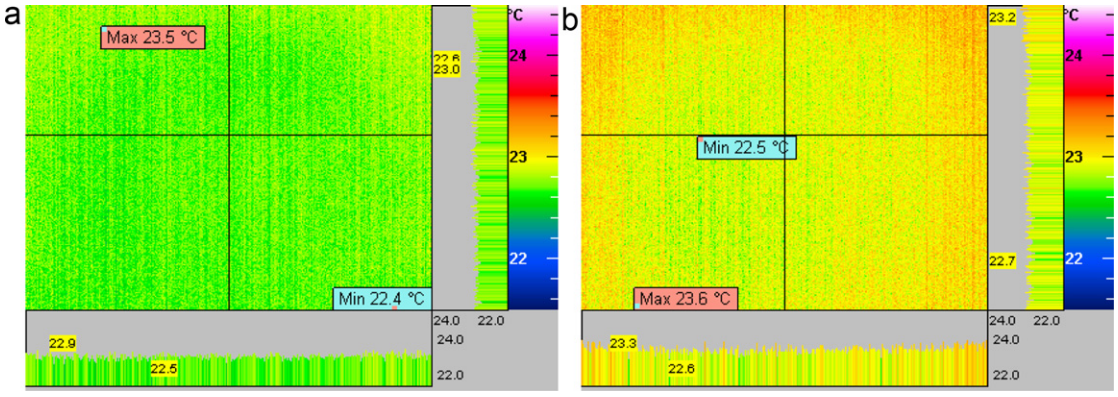

Fig. 8. Comparison of IR images for N117 MEA samples before and after degradation under idle conditions using 5% H_2 in N_2: (a) before degradation and (b) after degradation.

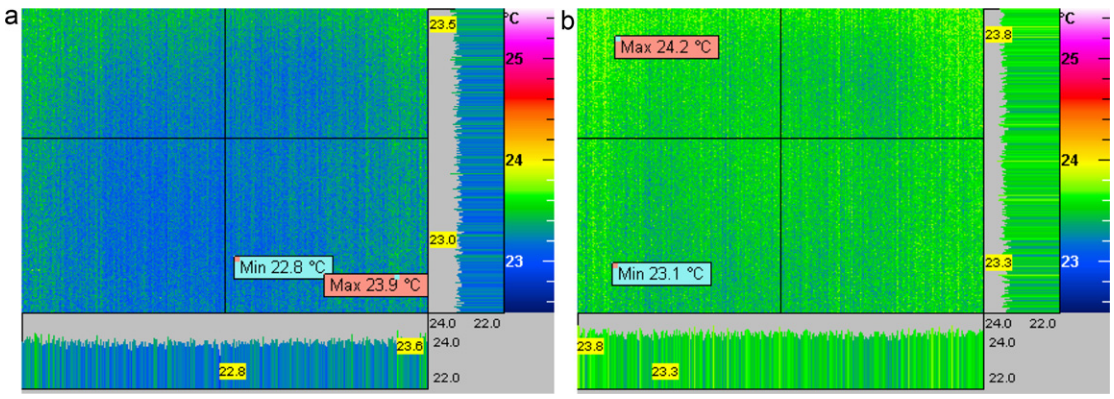

Fig. 9. Comparison of IR images for N115 MEA samples before and after degradation under idle conditions using 5% H_2 in N_2: (a) before degradation and (b) after degradation.

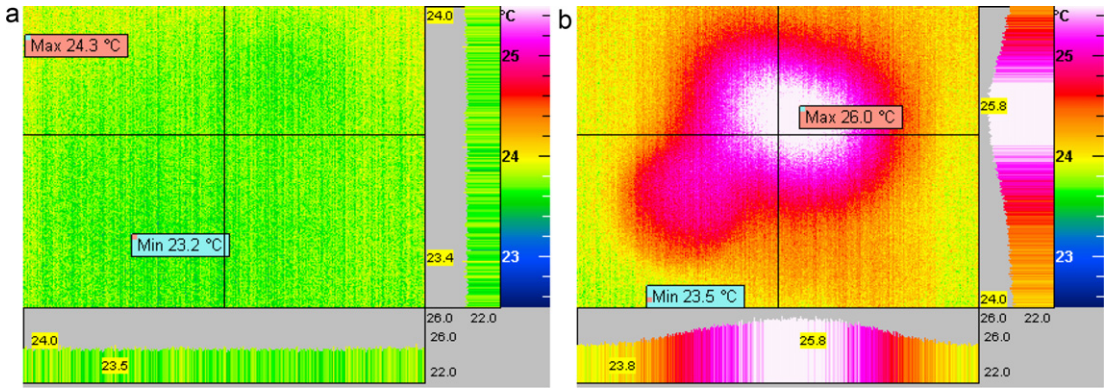

Fig. 10. Comparison of IR images for NR212 MEA samples before and after degradation under idle conditions using 5% H_2 in N_2: (a) before degradation and (b) after degradation.

Based on the experimental results, all the samples are categorized into these three permeability levels, as listed in Table 3. The high permeability of helium through degraded NR211 and NR212 further confirms the formation of pinholes during the 1000 h of operation under idle conditions.

3.2.3. *Loss of PTFE*

The most direct measurement of contact angle is achieved using the sessile drop method, where a drop of liquid is placed on a solid surface and the resulting angle formed between the plane of the solid and the tangent to the drop at the solid–liquid contact point is measured. This approach becomes complicated when the solid

Table 3
Overall comparison of fresh and degraded MEA permeability.

	Observation
MEA samples (fresh)	
N117	Non-permeable
N115	Less permeable
NR212	Less permeable
NR211	Less permeable
MEA samples (degraded)	
N117	Less permeable
N115	Less permeable
NR212	Highly permeable
NR211	Highly permeable

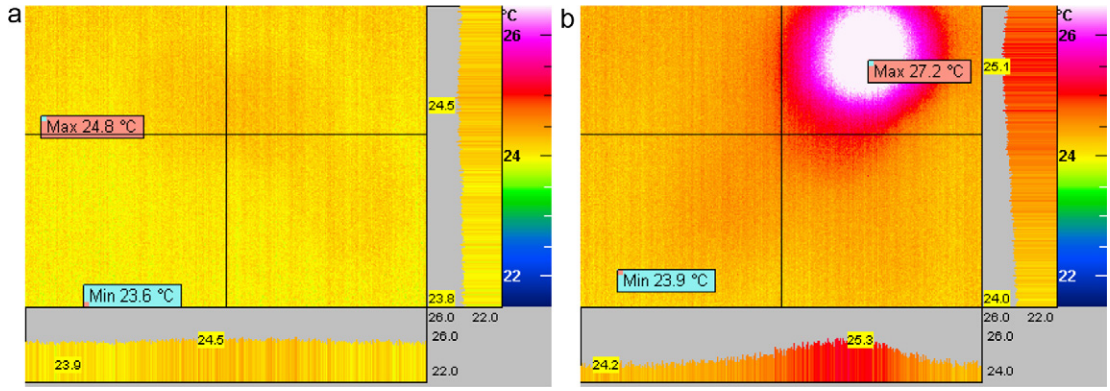

Fig. 11. Comparison of IR images for NR211 MEA samples before and after degradation under idle conditions using 5% H_2 in N_2: (a) before degradation and (b) after degradation.

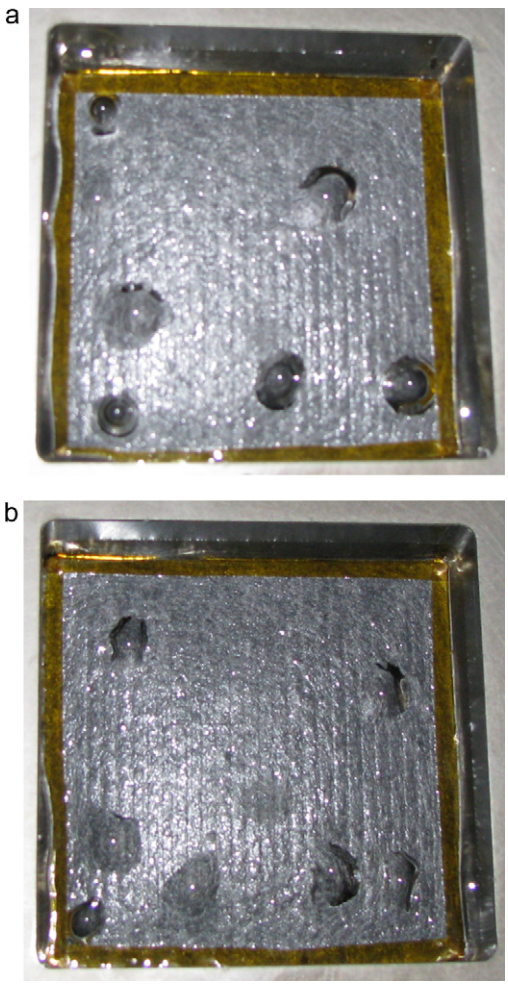

Fig. 12. Pictures of bubbles after 1000 h of degradation under idle conditions using 5% H_2 in N_2: (a) degraded NR211 and (b) degraded NR212.

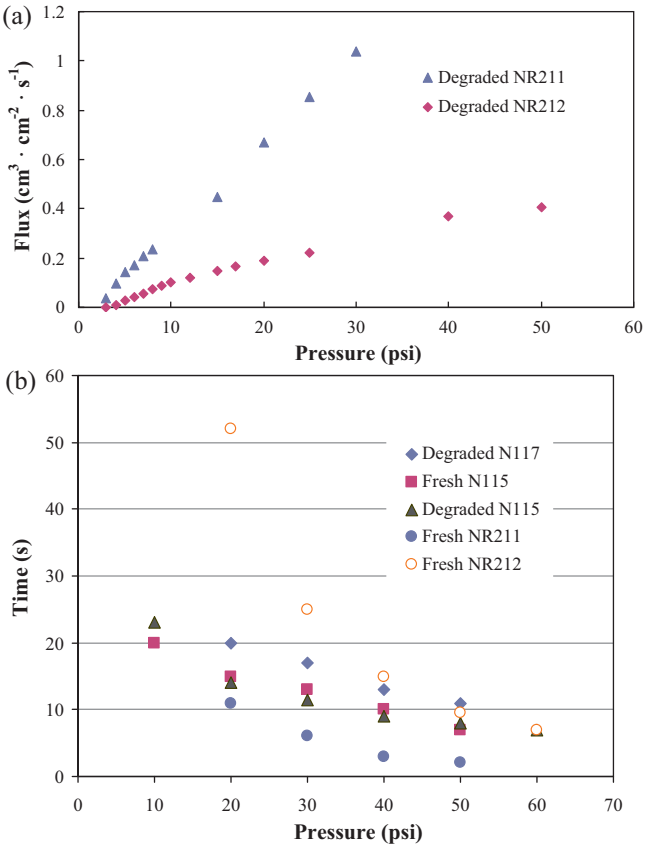

Fig. 13. Permeation of helium (a) through highly permeable MEAs and (b) through less permeable MEAs.

of interest is a porous medium. Due to the roughness and porosity of the surface, a droplet only contacts a fraction of the solid, causing the observed contact angle to deviate from the actual value. Despite such difficulties in measuring the actual value, contact angle can still be a useful qualitative tool for making direct comparisons between GDLs, such as comparisons of changes between fresh and degraded samples.

Table 4 shows that statistically, the contact angle of the fresh anode is about 2° higher than that of the cathode, as we used SGL 25DC (20% PTFE) for the anode and SGL 25BC (5% PTFE) for the cathode. After degradation, the contact angle for both the anode and the cathode decreases about 2°, indicating PTFE loss in the GDL for both sides during the degradation test as the hydrophobicity of the GDL is basically dependant on its PTFE content, and the more hydrophobic the GDL is, the more PTFE the GDL contains.

To obtain contact angle observations for the CLs, the GDL layers were peeled off carefully with the help of a scalpel, then the contact angles for the anode and cathode CLs were measured. However, from the data thus obtained (Table 5) we do not see any regular pattern of increase or decrease after degradation for the anode and cathode. This is probably due to unsuccessful peeling of the GDL from the MEA.

.

3.3. Modeling

The mechanism of membrane thinning can be understood through simulating Nafion weight loss during degradation testing. As the major reactants involved in the main chain unzipping process are the carboxyl end groups, their rate of weight loss was calculated in a wide range of concentrations, as shown in Fig. 14. A linear correlation was found between the loss rate and the carboxyl population, indicating that the initial amount of carboxyl groups present in the membrane determined the degradation rate of Nafion during the test. Moreover, such a linear correlation can also be noted from the release of the degradation products, as shown in Fig. 15. Fluoride ions had the highest emission rate, about two times higher than that of CO_2. In comparison, the amount of

Table 4
Comparison of contact angle change of GDLs.

	Fresh anode (°)	Fresh cathode (°)	Degraded anode (°)	Degraded cathode (°)
NR211	143.3	138.4	140.1	138.1
NR212	141.4	141.2	140.6	139.0
N115	143.1	140.9	139.6	136.0
N117	143.4	140.2	141.7	138.8
Average	142.8	140.2	140.5	138.0

Table 5
Comparison of contact angle change of CLs.

	Fresh anode (°)	Fresh cathode (°)	Degraded anode (°)	Degraded cathode (°)
NR211	142.7	137.0	142.3	138.6
NR212	132.7	135.4	138.7	144.7
N115	141.3	134.5	134.3	133.6
N117	140.3	131.9	133.3	129.3
Average	139.2	134.7	137.1	136.5

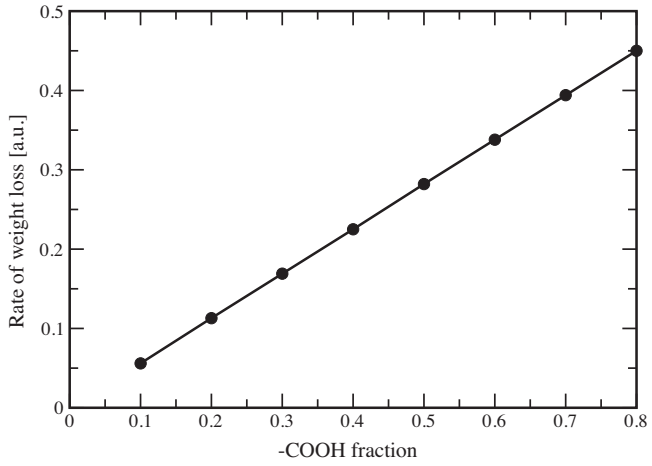

Fig. 14. Weight loss of degraded Nafion with various fractions of carboxyl end groups.

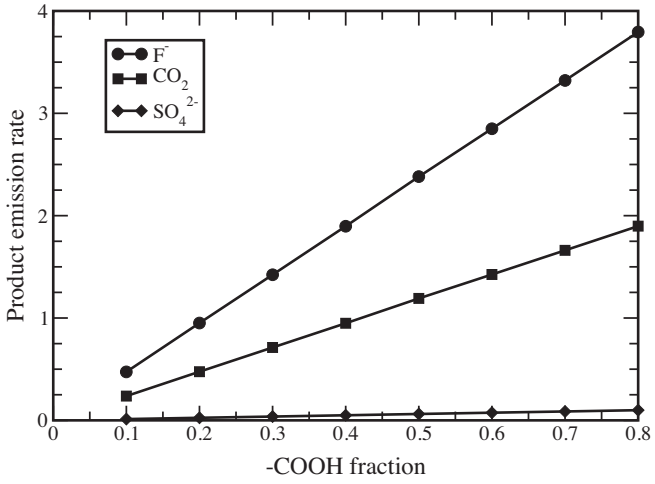

Fig. 15. Product emission rates of degraded Nafion with various fractions of carboxyl end groups.

reduced sulfate from Nafion side chains was negligible. One can expect that the loss of sulfonic groups, even in a small amount, may considerably decrease a Nafion membrane's proton conductivity. The evolution of $-SO_3H$ and –COOH end groups is thus computed

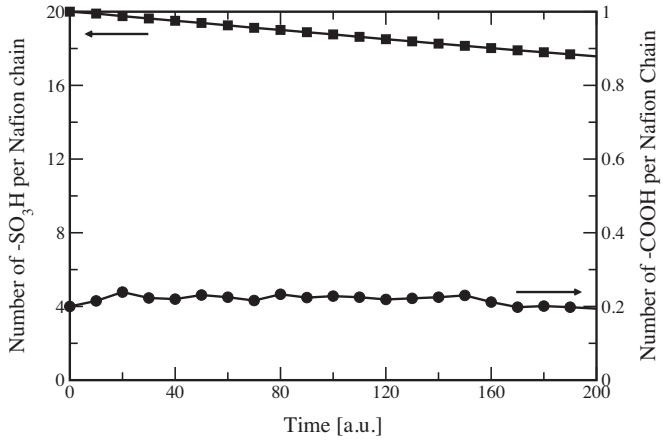

Fig. 16. The evolution of –COOH/$-SO_3H$ groups in degraded Nafion with 10% carboxyl end groups.

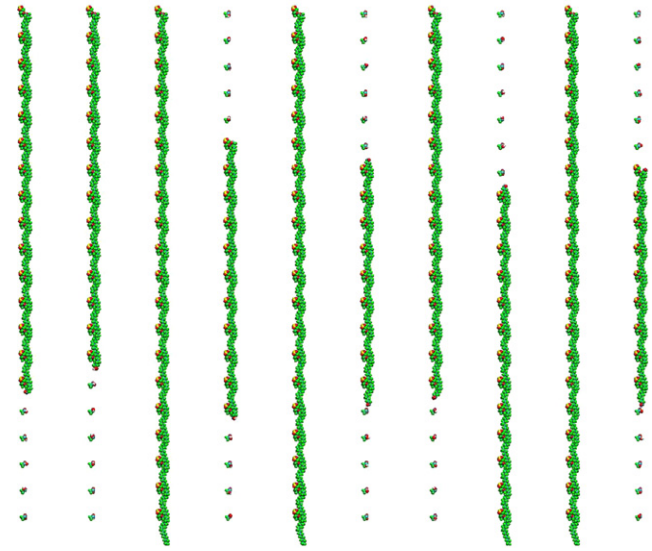

Fig. 17. Snapshot of degraded Nafion with 50% carboxyl end groups. The fragments left are trifluoroacetic acid.

in Fig. 16. It is interesting to note that the number of carboxyl groups remains constant, while a gradual decline in sulfonic groups occurs along with the testing time. The loss of sulfonic groups is attributed to the loss of Nafion side chains in the main chain unzipping process. The reason for the ineffective dissolution of carboxyl groups can be analyzed from the simulation snapshot shown in Fig. 17. As carboxyl groups are usually terminated at the ends of Nafion chains, the shrinkage of Nafion polymer takes place from the ends to the center. During this procedure, no additional carboxyl groups are created and the unzipping rate is basically proportional to the concentration of carboxyl end groups. Based on the present modeling results of Nafion degradation, it is known that the carboxyl defects, initially present in the membrane, are susceptible to radical attack.

4. Conclusions

Using a four-cell stack with Nafion membranes of different thicknesses, an accelerated stress test under idle conditions for 1000 h was carried out. The results indicate that under these conditions, membrane degradation is the major source of the overall cell performance degradation. The predominant reason for the drastic performance decay that occurred after 800 h for thinner membranes is the dramatic increase in hydrogen crossover, caused by significant membrane thickness loss and pinhole formation. Although the performance of thin membranes degrades much faster than that of thick membranes, the thickness loss for the former is lower, as thin membranes have less material to degrade. The mechanism of membrane thinning can be understood through the simulation of Nafion weight loss via main chain unzipping. Apart from membrane degradation, which is predominant in this accelerated degradation test under idle conditions, other degradation mechanisms also contribute to the total performance loss of the stack – for example, catalyst degradation (thickness loss in the CLs) and hydrophobicity loss in the GDL (contact angle decreases for both GDLs).

Acknowledgments

The authors acknowledge the NRC-Helmholtz Joint Research Program, NRC-MOST Joint Research Program, and NRC-IFCI's Internal Program for financial support.

References

[1] T. Payne, Fuel Cells Durability & Performance, US Brookline: The Knowledge Press Inc., 2009.
[2] H. Wang, H. Li, X.Z. Yuan, PEM Fuel Cell Failure Mode Analysis, CRC Press, 2011.
[3] DOE Cell Component Accelerated Stress Test Protocols for PEM Fuel Cells, http://www1.eere.energy.gov/hydrogenandfuelcells/fuelcells/components.html (March 2007).
[4] S. Sugawara, T. Maruyama, Y. Nagahara, S.S. Kocha, K. Shinohra, K. Tsujita, S. Mitsushima, K. Ota, J. Power Sources 187 (2009) 324–331.
[5] M.F. Mathias, R. Makharia, H.A. Gasteiger, J.J. Conley, T.J. Fuller, G.J. Gittleman, S.S. Kocha, D.P. Miller, C.K. Mittelsteadt, T. Xie, S.G. Yan, P.T. Yu, Electrochem. Soc. Interface 14 (2005) 24–35.
[6] J. Wu, X.Z. Yuan, J. Martin, H. Wang, D. Yang, J. Qiao, J. Ma, J. Power Sources 195 (2010) 1171–1176.
[7] X.Z. Yuan, S. Zhang, H. Wang, J. Wu, C. Sun, K.A. Friedrich, M. Schulze, A. Haug, J. Power Sources 195 (2010) 7594–7599.
[8] J. Wu, X.Z. Yuan, H. Wang, M. Blanco, J.J. Martin, J. Zhang, Int. J. Hydrogen Energy 33 (2008) 1735–1746.
[9] J. Wu, X.Z. Yuan, H. Wang, M. Blanco, J.J. Martin, J. Zhang, Int. J. Hydrogen Energy 33 (2008) 1747–1757.
[10] K.A. Friedrich, M. Schulze, A. Bauder, R. Hiesgen, I. Wehl, X.Z. Yuan, H. Wang, ECS Trans. 25 (2009) 395–403.
[11] R. Hiesgen, I. Wehl, K.A. Friedrich, M. Schulze, A. Haug, A. Bauder, A. Carreras, X.Z. Yuan, H. Wang, ECS Trans. 28 (2010) 79–84.
[12] S. Zhang, X.Z. Yuan, J. Ng Cheng Hin, J. Wu, H. Wang, K.A. Friedrich, M. Schulze, J. Power Sources 195 (2010) 1142–1148.
[13] X.Z. Yuan, S. Zhang, J. Wu, H. Wang, in: H. Wang, H. Li, X.Z. Yuan (Eds.), PEM Fuel Cell Diagnostic Tools, CRC Press, 2011.
[14] V. Uvarov, I. Popov, Mater. Charact. 58 (2007) 883–891.
[15] P.J. Ferreira, G.J. la O', Y. Shao-Horn, D. Morgan, R. Makharia, S. Kocha, H.A. Gasteiger, J. Electrochem. Soc. 152 (2005) A2256–A2271.
[16] R. Lin, E. Gülzow, M. Schulze, K.A. Friedrich, J. Electrochem. Soc. 158 (2011) B11–B17.
[17] A.C. Fernandes, E.A. Ticianelli, J. Power Sources 193 (2009) 547–554.
[18] A.P. Young, J. Stumper, E. Gyenge, J. Electrochem. Soc. 156 (2009) B913–B922.
[19] D.L. Wood, J.R. Davey, P. Atanassov, R.L. Borup, ECS Trans. 3 (2006) 753–763.
[20] R. Lin, B. Li, Y.P. Hou, J.X. Ma, Int. J. Hydrogen Energy 34 (2009) 2369–2376.
[21] A. Haug, R. Hiesgen, M. Schulze, G. Schiller, in: H. Wang, H. Li, X.Z. Yuan (Eds.), PEM Fuel Cell Diagnostic Tools, CRC Press, 2011.
[22] M. Schulze, A. Haug, in: H. Wang, H. Li, X.Z. Yuan (Eds.), PEM Fuel Cell Diagnostic Tools, CRC Press, 2011.
[23] S. Kundu, M.W. Fowler, L.C. Simon, R. Abouatallah, N. Beydokhti, J. Power Sources 183 (2008) 619–628.
[24] S. Kundu, K. Karan, M. Fowler, L.C. Simon, B. Peppley, E. Halliop, J. Power Sources 179 (2008) 693–699.
[25] A. Chatterjee, D. Vlachos, J. Comput. Aided Mater. Des. 14 (2007) 253–308.
[26] D.E. Curtin, R.D. Lousenberg, T.J. Henry, P.C. Tangeman, M.E. Tisack, J. Power Sources 131 (2004) 41–48.
[27] F.D. Coms, ECS Trans. 16 (2008) 235–255.
[28] M. Takasaki, K. Kimura, K. Kawaguchi, A. Abe, G. Katagiri, Macromolecules 38 (2005) 6031–6037.
[29] A. Collier, H. Wang, X.Z. Yuan, J. Zhang, D.P. Wilkinson, Int. J. Hydrogen Energy 31 (2006) 1838–1854.